Contents lists available at ScienceDirect

Transactions of Nonferrous Metals Society of China

36(2026) 337−354

www.tnmsc.cn

Microstructure and mechanical properties evolution of Al−Mg−Sc−Zr alloy fabricated by laser powder bed fusion

Xiang LI [a,b], Zheng-jiang GAO [c,*], Yun-zhong LIU [a,b,**]

[a] Guangdong Provincial Key Laboratory for Processing and Forming of Advanced Metallic Materials, South China University of Technology, Guangzhou 510640, China;

[b] National Engineering Research Center of Near-net-shape Forming for Metallic Materials, South China University of Technology, Guangzhou 510640, China;

[c] Key Laboratory of Advanced Functional Materials, Ministry of Education, Beijing University of Technology, Beijing 100124, China

Abstract: The densification characterization, phase constitution, precipitation evolution and mechanical performance of Al−Mg−Sc−Zr alloy processed by laser powder bed fusion (LPBF) were systematically investigated. Moreover, the evolution of phase constitution and precipitation behavior after heat treatment were characterized by using X-ray diffraction (XRD) and transmission electron microscope (TEM) analysis. The ultimate tensile strength (UTS) of as-built samples ranged from 396.8 to 414.6 MPa as the scanning speed decreased from 1600 to 1000 mm/s. After post heat treatment, the yield strength (YS) increased to (513.1±1.3) MPa, while the UTS increased from (414.6±5.1) to (539.2±1.5) MPa. The significant improvement of mechanical performance was ascribed to the formation of secondary $Al_3(Sc,Zr)$ precipitates.

Keywords: additive manufacturing; laser powder bed fusion; Al−Mg−Sc−Zr; precipitation behavior; microstructure; mechanical performance

1 Introduction

Laser powder bed fusion (LPBF) is widely used in many fields such as aerospace, medical equipment, and automobile owing to its significant merits in fabricating complex structure parts [1]. Due to their low density, LPBF fabricated aluminum (Al) alloys with outstanding mechanical performance are strongly expected, particularly in aerospace and military fields [2,3]. However, only a small amount of castable Al alloys is suitable for additive manufacture process because of their small solidification window and low hot-cracking susceptibility. Up to now, 2xxx, 6xxx and 7xxx series Al alloys are usually fabricated by traditional techniques, i.e., cast, wrought and welding, while they exhibit intensive hot-cracking susceptibility during LPBF process [4,5]. Thereby, investigations on the LPBF fabricated Al alloys majorly concentrate on the castable Al−Si series alloys (e.g. Al7Si, AlSi10Mg and Al12Si) [6]. The Al−Si series alloys with near-eutectic composition indicate that they exhibit a narrow freezing range during solidification, resulting in the low susceptibility of hot-cracking.

Though LPBF fabricated Al−Si series alloys demonstrate excellent processability, they cannot

Corresponding author: *Zheng-jiang GAO, E-mail: gaozj@avimetalam.com;
**Yun-zhong LIU, Tel/Fax: +86-20-87110081, E-mail: yzhliu@scut.edu.cn

https://doi.org/10.1016/S1003-6326(25)66968-8

Received 11 March 2024; accepted 30 August 2024

compete with the extensively used high-strength 2xxx and 7xxx Al alloys owing to their limited strength. This dilemma cannot satisfy the ever-growing strength requirements of aerospace fields. Now, only simple and small-size 2xxx and 7xxx Al alloy counterparts can be directly fabricated by LPBF [7,8]. Additionally, LPBF fabricated Al alloys exhibit the potential to substitute titanium (Ti) alloy and steel to meet the aim of lightweight and energy saving [9]. Thereby, LPBF fabricated Al alloys with excellent printability and high performance are significantly desirable and expected.

A promising alternative to 2xxx and 7xxx Al alloys is Al−Mg−Sc−Zr alloy. With moderate strength, its strength mainly depends on the solid-solution and precipitation strengthening [10,11]. Notably, with the modification of Sc and Zr, the Al_3(Sc,Zr) phase could be produced, promoting significant grain refinement and precipitation strengthening [12]. In recent years, extensive studies have concentrated on cast and wrought Al−Mg−Sc−Zr alloy, which demonstrates excellent room temperature mechanical performance and significant resistance to recrystallization [13]. Thereafter, investigations concentrated on LPBF fabricated Al−Mg−Sc−Zr alloy have become a research hotspot in recent decades. SHI et al [14] investigated the printability of Al−Mg−Sc−Zr alloy and fabricated dense and crack-free samples, identifying that Al−Mg−Sc−Zr alloy was suitable for LPBF additive manufacturing. SPIERINGS et al [15] studied the microstructural features of Al−Mg−Sc−Zr alloy fabricated by LPBF, demonstrating that fine equiaxed grains formed near the melt pool bottom and coarse columnar grains grew towards the building direction. Importantly, the tensile performance could be further improved after aging treatment because of the nano-scale Al_3(Sc,Zr) precipitation formation, promoting considerable precipitation strengthening. Moreover, the static mechanical performance in various orientations was studied by SCHMIDTKE et al [16], identifying that the tensile strength of heat-treated samples can exceed 500 MPa for all directions. SPIERINGS et al [17] focused on the mechanical performance of LPBF fabricated Al−Mg−Sc−Zr alloy and identified outstanding tensile performance of ~400 MPa for as-built samples. Furthermore, the strength of heat-treated samples can exceed 500 MPa, demonstrating that heat treatment is an important post-process technique to improve the mechanical performance of Al−Mg−Sc−Zr alloy. Nevertheless, the process efficiency of the LPBF technique is still relatively low which is proportional to the laser scanning speed [18]. The reason could be attributed to the fact that current LPBF technology is a layer-by-layer deposition process with the use of low laser power (50−400 W) coupled with low scanning speed (80−1400 mm/s), limiting the efficiency of processing large-scale engineering components [19]. Considering the ever-increasing strength and cost requirements of aerospace fields, it is worth further studying the microstructural feature and mechanical performance of Al−Mg−Sc−Zr alloy especially fabricated at different laser scanning speeds. Moreover, the precipitation behavior of Al−Mg−Sc−Zr alloy corresponding to different laser scanning speeds also needed to be elucidated.

In this study, the densification behavior and microstructure evolution of samples fabricated at different laser powers and scanning speeds were studied, and the underlying mechanisms were also analyzed. The influence of laser scanning speeds on microstructure evolution and mechanical properties was also systematically studied. Furthermore, the tensile performance of as-built and heat-treated samples was identified to reveal the precipitate behavior of secondary Al_3(Sc,Zr) nano-precipitates.

2 Experimental

2.1 Raw powders

Argon gas atomized pre-alloyed powders with the particle size ranging from 30 to 72 μm were used as raw materials, as shown in Fig. 1. The chemical composition of raw materials and as-built samples were measured by inductively coupled plasma atomic emission spectroscopy (ICP-OES) and the corresponding results are summarized in Table 1. To eliminate the moisture, the original powder feedstocks were dried at 120 °C for 12 h before LPBF processing.

2.2 Sample preparation and post heat treatment

Sample preparation experiment was conducted in a commercial EOSINT M280 powder-bed instrument, including a Yb-fiber laser with 400 W maximum power (spot size of around 100 μm, and

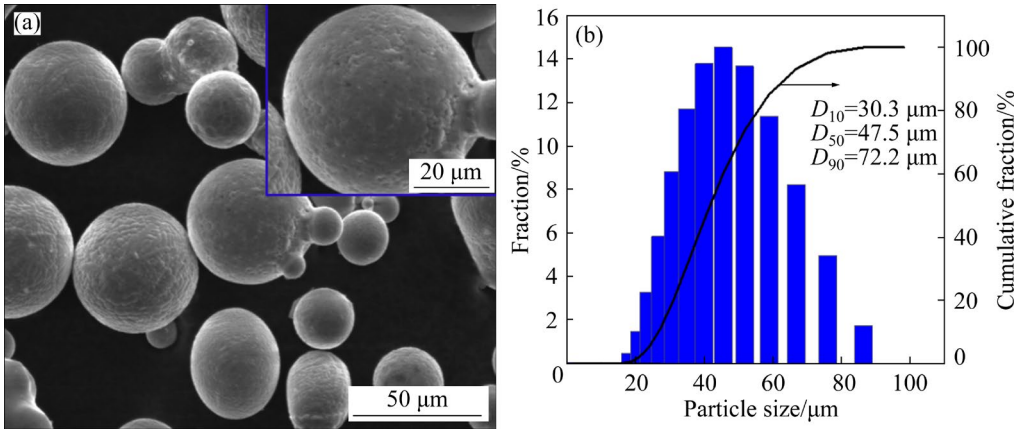

Fig. 1 (a) Morphology of Al−Mg−Sc−Zr pre-alloyed powders revealed by scanning electron microscopy (SEM); (b) Powder size distribution

Table 1 Chemical compositions of original feedstocks and as-built specimens (wt.%)

Material	Mg	Mn	Sc	Zr	Si	Cu	Ti	Fe	O	Al
Original feedstock	4.84	0.50	0.66	0.33	0.055	0.001	0.004	0.31	0.038	Bal.
As-built specimen	4.33	0.48	0.66	0.33	0.030	0.001	0.003	0.080	–	Bal.

wavelength of 1064 nm). For process parameter optimization, test samples (9 mm × 9 mm × 7 mm) were processed at different combinations of laser power and scanning speed ranging 221−370 W and 500−3000 mm/s, respectively. The powder layer thickness and hatch distance were kept at 30 and 100 μm for all the processes. All samples were fabricated with a 67° rotation angle alternating strategy as presented in Fig. 2. The LPBF process was conducted in an argon protective atmosphere under a controlled minimum oxygen content (0.1 vol.%). Archimedes law was used to determine the densification of the specimens. Ten tests were carried out for each sample. To obtain the fully dense and crack-free samples, the optimized laser power (P) and scanning speed (V) were 370 W and 1200 mm/s, respectively. 5083 Al substrate was used and preheated to 180 °C before the LPBF processing. During the LPBF processing, deposition was opposite to the protective gas flow direction in order to minimize splashing. The heat-treated specimens were first aged for 325 °C for 4 h and then cooled to room temperature in air.

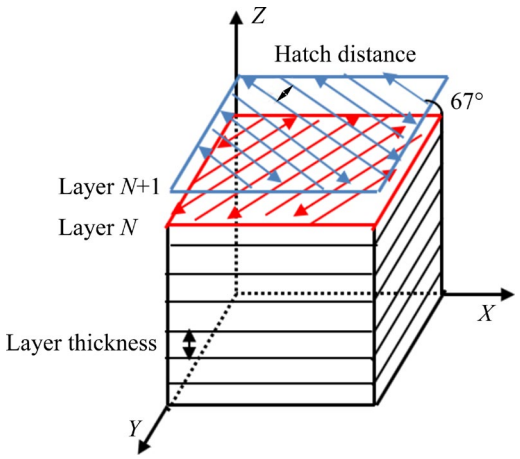

Fig. 2 Schematic graph of building direction and laser scanning strategy

2.3 Microstructure characterizations and mechanical performance tests

Pore characterization investigations were carried out by optical microscopy (OM, Leica DMI5000 M). For OM observation, the metallographic sample was first mechanical ground and then polished. A Nova Nano SEM 430 scanning electron microscopy (SEM, FEI, Holland) was used in this study. Moreover, energy dispersive spectroscopy (EDS) and electron backscatter diffraction (EBSD) detectors were included in the SEM. For SEM characterization, the specimens were first mechanical ground and polished. Keller reagent (2.5 mL HNO_3, 1.5 mL HCl, 1 mL HF and 95 mL deionized water) was used to reveal the microstructural feature. X-ray diffraction (XRD, PANalytical, Holland) with Cu K_α radiation was

conducted to complete the phase analysis at a working voltage of 40 kV. The scanning rate of 12 (°)/min was used for the XRD patterns in the 2θ range from 20° to 120°. For EBSD tests, the mechanically polished specimens were further ion-polished at a working voltage of 3.5−5.5 kV for 1 h. The nanoscale microstructure analyses were carried out via transmission electron microscope (TEM, JEOL JEM−2100F) coupled with EDS at an operating voltage of 200 kV. For TEM observation, the lamina was cut to 0.5 mm thick slices via electric discharge machining (EDM). Ion polishing system (Gatan 695) was used to further process the TEM slices.

Before the microhardness tests, all specimens were mechanically ground and polished to the surface roughness of 1 μm surface. Vickers microhardness identifications were conducted via a DHV−1000Z Vickers microhardness instrument under a 200 g load and a 15 s dwell time. To minimize the error, 15 tests were carried out for each condition. Tensile experiments were performed along the horizontal direction of each specimen with the gauge size of 14 mm × 3 mm × 2 mm, as presented in Fig. 3. For all tests, a crosshead speed of 0.5 mm/min was used in a Shimadzu AGXplus tester at room temperature. Three specimens were measured to ensure statistical consistency. Then, the tensile fracture morphologies were observed by SEM.

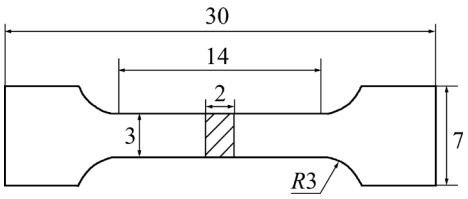

Fig. 3 Drawing of tensile sample (Unit: mm)

3 Results

3.1 Relative density and processability

The relative density of the as-built specimens by different processing parameters is shown in Fig. 4. Figure 4(a) presents the relative density varied with laser powder at the constant scanning speed of 1600 mm/s. Obviously, the relative density raised continually from 95.2% to 98.1% as the laser

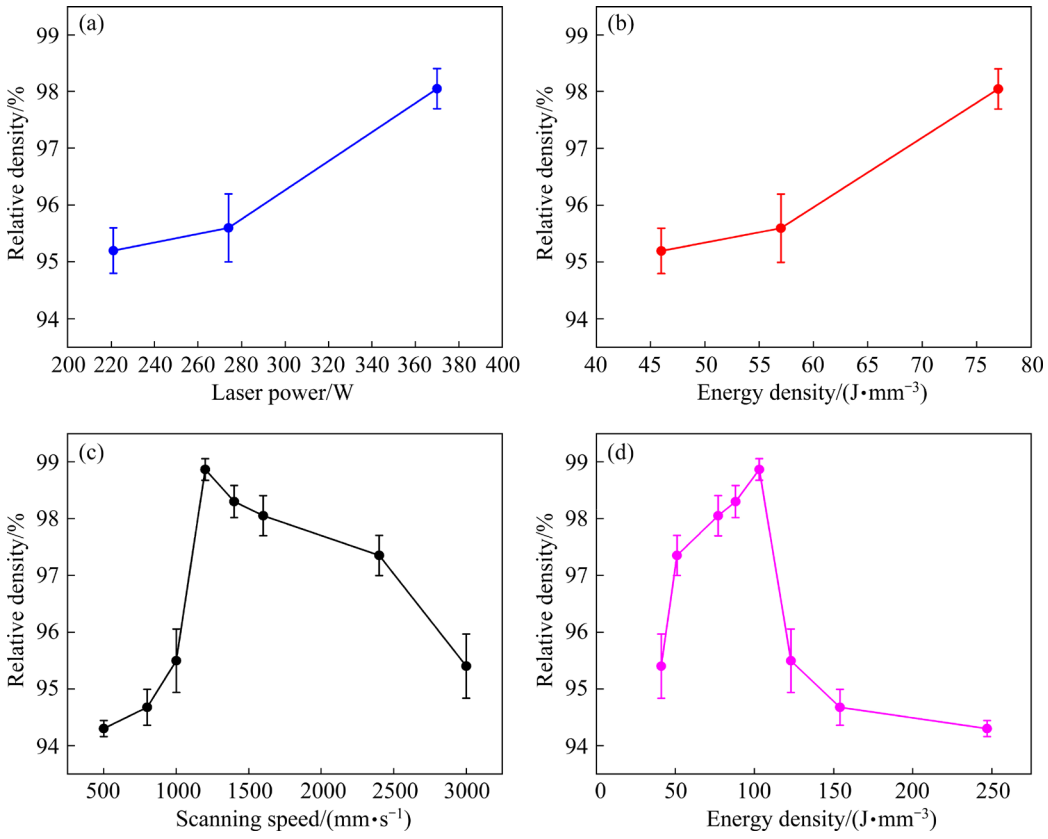

Fig. 4 Relative density of as-built specimens obtained at different process parameters: (a) Laser power (constant scanning speed of 1600 mm/s); (b) Energy density (constant scanning speed of 1600 mm/s); (c) Scanning speed (constant laser power of 370 W); (d) Energy density (constant laser power of 370 W)

power increased, viz., increasing the laser energy density (Fig. 4(b)). The result shows that the pores could be eliminated and there was a tendency that the proportion of pore reduced as the laser power increased. Generally, with the increment of laser energy density, the melt pool enlarged, contributing to lower porosity and higher relative density [20]. A high energy density increased the melt pool size, thus the overlap portion between adjacent scanning tracks and deposition layers was enhanced and the pore was reduced. For the track-by-track and layer-by-layer deposition manner of LPBF, an adequate overlap proportion is important for high densification.

In contrast, for the constant laser power (370 W), the densification primarily increased and then dropped with the increment of scanning speed, viz., decreasing the laser energy density. Thereby, the lowest porosity and the highest relative density were achieved at 1200 mm/s (Fig. 4(c)). It is worth noting that the high reflectivity intrinsic to aluminum alloy powders might contribute to the insufficiency of laser energy input, resulting in insufficient melt of raw powders. However, the high laser power (370 W) guaranteed an adequate laser energy input, resulting in high temperature within the melt and promoting the break of oxide film and decrement of liquid dynamic viscosity (μ) [21]. Generally, a smaller μ ensured an adequate spread of melt on the former deposited layer, promoting the wettability and densification. The wettability of liquid, which was dependent on the interaction of powders and laser, had a significant influence on the inter-layer integrating level.

The corresponding optical micrograph images also reveal the pore types and densification behavior of samples fabricated with different scanning speeds. The optical images of as-built specimens fabricated at various scanning speeds are presented in Fig. 5.

Obviously, large-sized spherical pores and large cavities appeared at a relatively small scanning speed (500 mm/s), indicating poor densification of as-built samples. As the scanning speed was relatively small, the laser beam dwelling lifetime became longer, stimulating the melt superheating. This intensified the element vaporization, inducing pore defects and decreasing the densification. Additionally, the gap between melting and solidifying became longer at a low scanning speed, leading to a more marked growth of trapped hydrogen pore and a low densification level [22]. As the scanning speeds rose to 1600 mm/s, the large-size pores transformed to some small-size pores. Specially, the as-built sample was nearly fully dense and free of big pores at 1200 mm/s. This identified that a threshold of scanning speed existed to yield a maximum relative density. While the scanning speeds raised from 1600 to 2400 mm/s, the pore size and portion increased again. Notably, the capillary instability within the melt pool intensified when the scanning

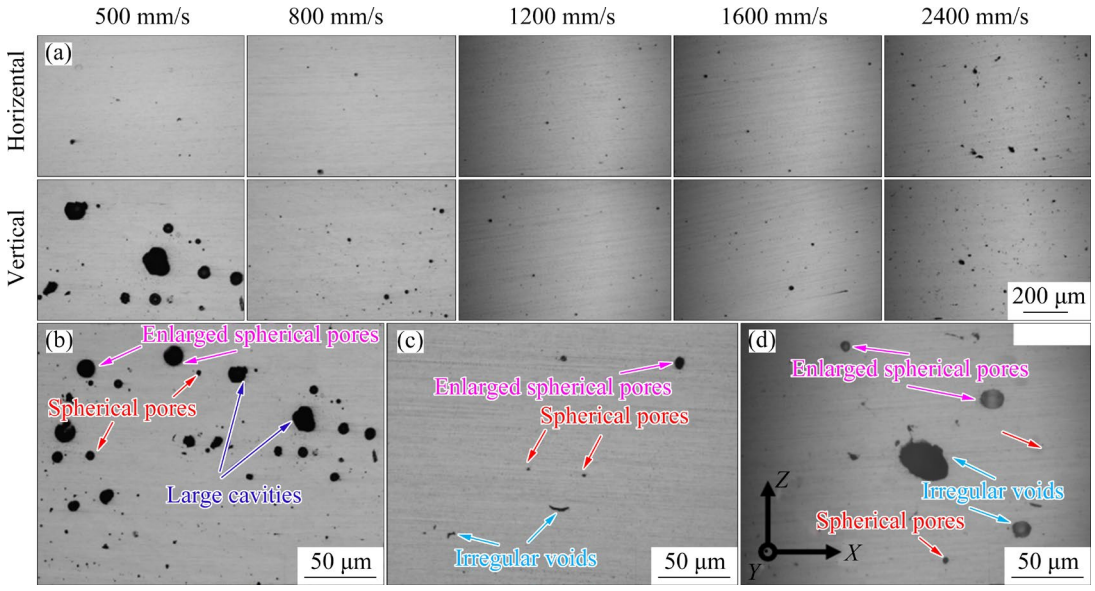

Fig. 5 Optical micrographs revealing densification behaviors of samples fabricated at various scanning speeds: (a) Horizontal and vertical images of all specimens; (b−d) Magnified images at various scanning speeds of 500 mm/s, 1600 mm/s and 2400 mm/s, respectively

speed was relatively high, contributing to the balling effect due to the splashing of liquid droplets [23]. The balling effect led to the rough surface, preventing the adequate spread of liquid on the former deposited layer. As a result, the densification lowered. However, the cracks were not found within the current samples. The above relative density data and the corresponding optical micrograph images identified that Al−Mg−Sc−Zr alloy demonstrated excellent processability, and fully dense and crack-free specimens could be processed at a wide process window.

3.2 Phase constitution

The XRD patterns of raw powders and as-built samples are depicted in Fig. 6. The diffraction peaks of the α(Al) phase were observed in the whole XRD patterns. However, $Al_3(Sc,Zr)$ and other new phases were not detected owing to the limited phase fraction and XRD detection limitation.

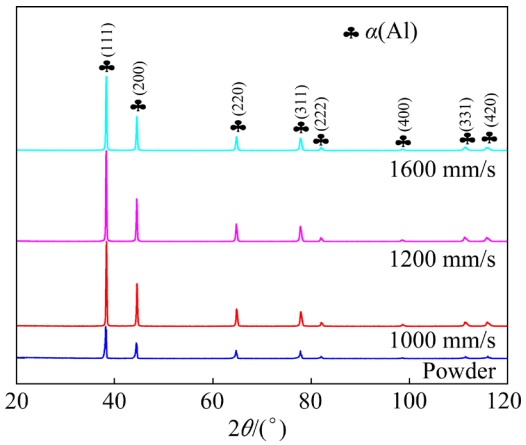

Fig. 6 XRD patterns of raw powders and as-built samples fabricated at various scanning speeds (2θ=20°−120°)

It can be deduced that periodic rapid melting and solidifying of LPBF suppress the precipitation of secondary phase and increase the solubility limitation of solutes within the matrix. The XRD pattern of raw powders demonstrated an obvious (111) texture. In contrast, the XRD patterns of as-built samples illustrated intensive (200) diffraction peaks compared with raw powders, indicating a marked texture transformation owing to the rapid cooling feature intrinsic to LPBF. The (200) texture is ascribed to the preferred solidification direction of ⟨100⟩ in aluminum [24]. This characteristic of obvious (200) texture can also be found in AlSi10Mg and Al−12Si alloys [25].

To further analyze the XRD diffraction peaks, the XRD patterns within a narrow 2θ range of 37.5°−39.0° and 44.0°−45.0° are shown in Fig. 7.

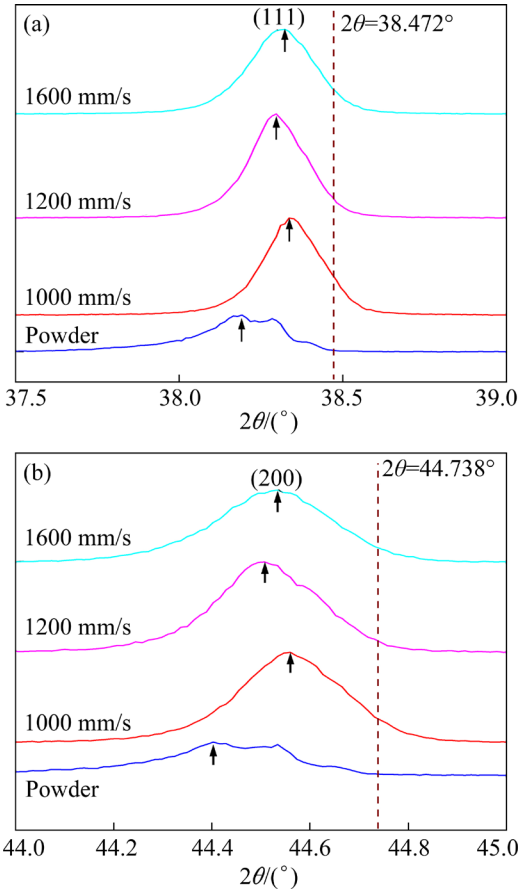

Fig. 7 Magnified view of XRD patterns showing variation of diffraction peaks at various scanning speeds: (a) (111) peak; (b) (200) peak

As depicted in Fig. 7, the XRD patterns revealed that the 2θ position of diffraction peaks shifted with the increment of scanning speed. Here, the reference α(Al) diffraction peaks (JCPDS Card No. 04-0787, 2θ=38.472° and 2θ=44.738°) were used as a comparison. Compared with the reference diffraction peaks, the location of the 2θ deflected to a lower angle, implying the lattice distortion of α(Al) phase. However, the 2θ values of as-built samples processed at all laser scanning speeds considerably increased compared with the original powders. The corresponding results of the identified XRD diffraction peaks are summarized in Table 2.

According to the Bragg's law [26], there is

$$2d\sin\theta=n\lambda\ (n=1, 2, 3, \cdots) \quad (1)$$

where λ represents the XRD diffraction wavelength; d and θ are the lattice plane distance of (hkl) and the angle of diffraction peak, respectively. The diffraction peak deflected to a smaller value indicating a greater d, which was attributed to the solid solution of Mg [27]. Compared with the raw powders, the 2θ values of as-built samples were much higher, which might be produced by the Mg volatilization. The dramatically high temperature within the melt pool led to a significant evaporation loss of Mg due to the higher vapor pressure, decreasing the Mg content within the matrix. Thereby, Mg content in as-built specimens decreased compared with raw powders, resulting in the decrease of d value (Table 2).

Table 2 XRD results revealing location and intensity variation of α(Al) diffraction peaks

Specimen	2θ/(°)	d/Å	a/Å	Intensity
Standard card (No. 04-0787)	38.472	2.3380	4.0495	–
Raw powder	38.191	2.3546	4.0783	3161
As-built (1000 mm/s)	38.337	2.3459	4.0632	8363
As-built (1200 mm/s)	38.297	2.3483	4.0674	8971
As-built (1600 mm/s)	38.323	2.3468	4.0648	7312

a−Lattice parameter

3.3 Microstructure of as-built samples

Figure 8 shows the backscattered SEM images of melt pool morphologies in the building direction. Obviously, the configurations of melt pool were significantly influenced by the scanning speeds. Specially, typical fan-shell microstructure was found, which included two distinct regions in each melt pool: coarse columnar grain within the center of molten pool and fine equiaxed grain near the molten pool bottom. The fine equiaxed grain formation was ascribed to the introduction of Al_3(Sc,Zr) nucleating agents, refining the α(Al) grains [28]. In contrast, the columnar grain formation was ascribed to the thermal behavior of LPBF and the absence of nucleating agents during solidification [15,26]. Notably, bright contrast particles could be observed near the molten pool bottom (Fig. 8(d)). Moreover, only a few of bright contrast particles could be found within the molten pool center, identifying an uneven distribution of

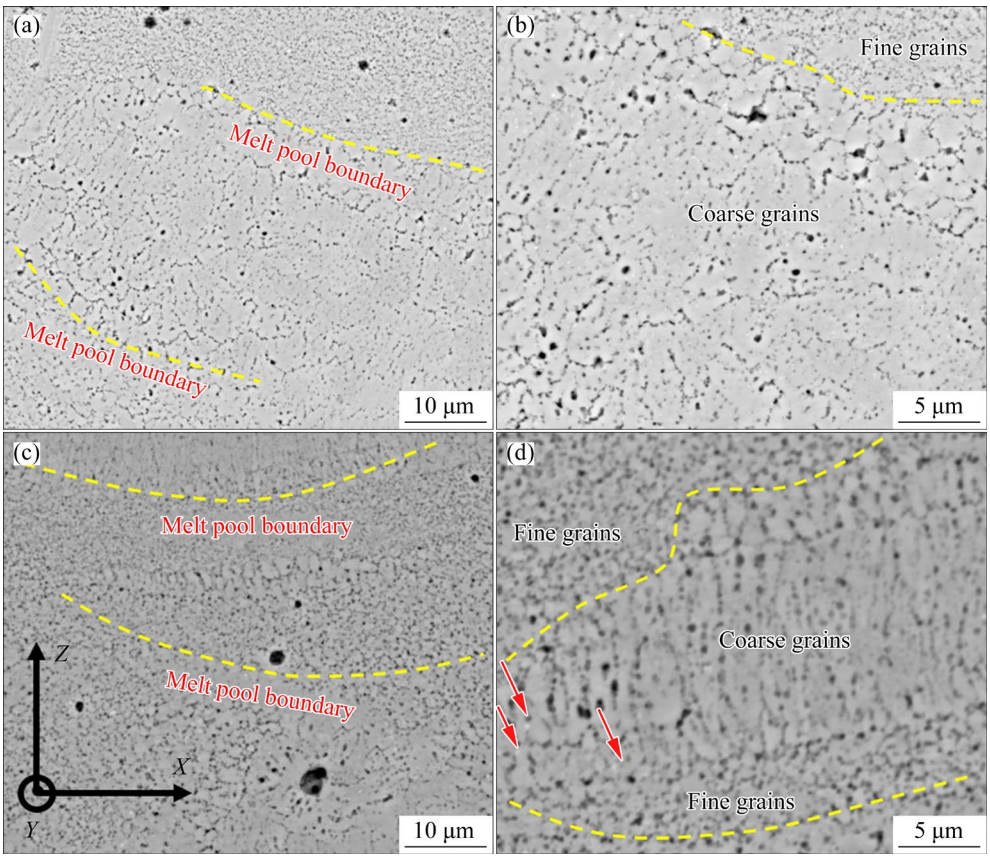

Fig. 8 Backscattered SEM micrographs revealing melt pool morphologies of samples fabricated at different scanning speeds: (a, b) 1000 mm/s; (c, d) 1200 mm/s

particles within the melt pool. Generally, the LPBF fabricated Al−Mg−Sc−Zr alloy majorly contains two kinds of phase: Al−Mg oxide and $Al_3(Sc,Zr)$ [28]. In backscattered SEM images, elements with greater atomic number would exhibit brighter contrast, and thereby above bright contrast particles might be $Al_3(Sc,Zr)$ precipitates, produced during the solidification. These $Al_3(Sc,Zr)$ phases demonstrate a similar lattice structure with α(Al), stimulating the heterogeneous nucleation. By comparing the melt pool morphologies and grain distribution of various specimens, the fine-grain areas of specimens fabricated at 1200 mm/s were greater than those at 1000 mm/s, which might be attributed to the various solidification rates and precipitation behaviors [26].

To further reveal the grain feature, the inverse polar figure (IPF) map of sample fabricated at 1200 mm/s is presented in Fig. 9. A significant bimodal or heterogeneous grain microstructure was observed, fine equiaxed grains aggregated along melt pool bottom and coarse columnar grains grew toward building direction. The transformation of grain morphology could be ascribed to various temperature distributions and precipitate behaviors of secondary phase particles within the melt pool [12,15]. Notably, the proportion of secondary phase particles in the fine equiaxed grain regions is much greater compared with columnar grain zones, as presented in Fig. 8(d). EBSD results also identified that no distinct texture existed in the fine equiaxed grain regions due to disordered fine grains, while significant ⟨001⟩ solidification fiber texture was observed in columnar grain zones (Fig. 9(a)).

The grain size distribution is plotted in Figs. 9(c, d). Obviously, the grain size in columnar grain zones ranged from 1 to 10 μm, while the grain size in equiaxed grain bands ranged from 1 to 7 μm. Notably, the proportion of the equiaxed grains was about 23% retrieved from the EBSD statistical results, which was smaller than that of LPBF fabricated Al−Mg−Sc−Zr alloy (~42%) in the work of WANG et al [12] and Al−Mn−Mg−Sc−Zr alloy (~60%) reported by JIA et al [5]. The variation in the proportion of equiaxed grain might be due to various alloy compositions and process parameters.

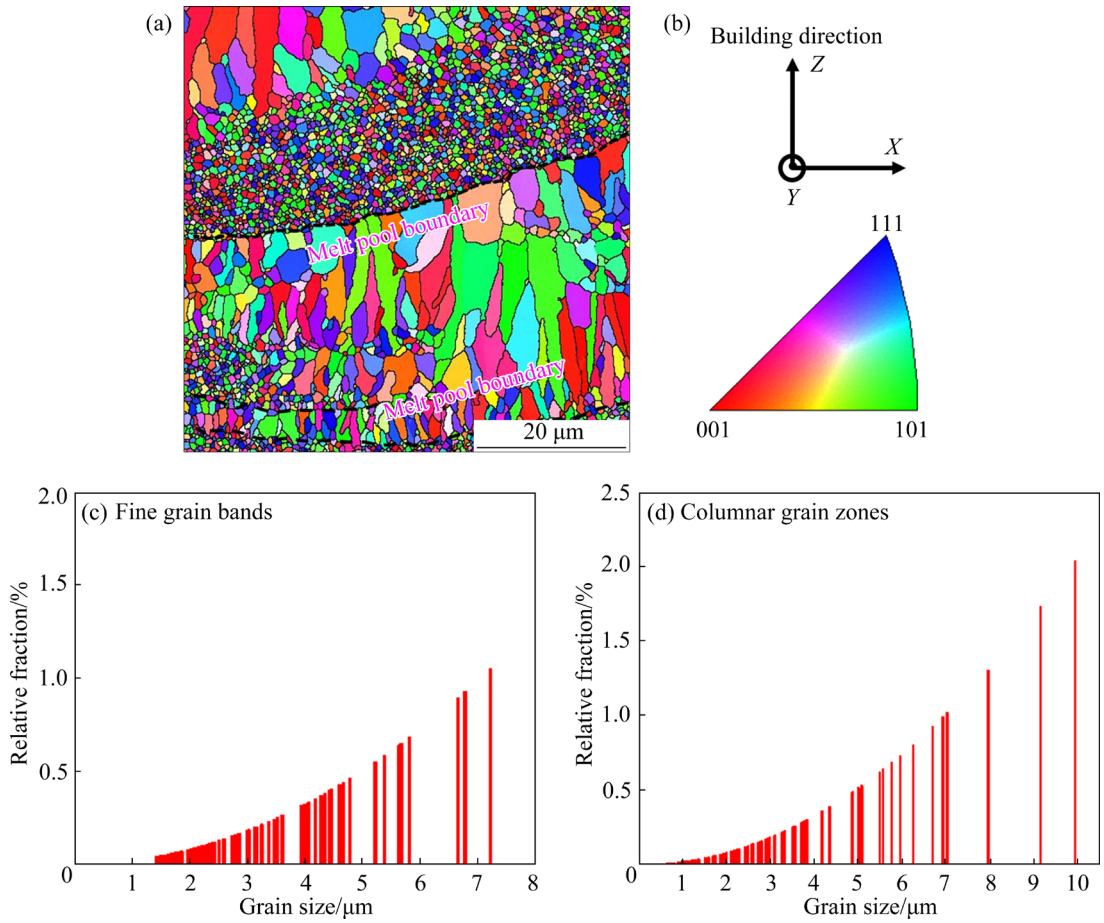

Fig. 9 Microstructure feature of LPBF sample fabricated at 1200 mm/s: (a) Inverse polar figure; (b) Illustration of building direction; (c, d) Grain size distributions of fine grain bands and columnar grain zones, respectively

The microstructure and major element distributions were further revealed via TEM and EDS mapping, as presented in Fig. 10. HAADF-STEM image reveals detailed grain microstructure and key element distributions of Al, Mg, Mn, Sc and Zr. The STEM image presents an uneven distribution of secondary phase particles, namely, their abundance in equiaxed grain areas and their absence in coarse columnar grain zones. These secondary phase particle sizes ranged from nanometer to submicron. The EDS mappings showed that Al and Mg had uniform distribution in the matrix (Figs. 10(b, c)).

In contrast, the secondary phase particles demonstrated a distinct Sc and Zr aggregation, attributing to primary $Al_3(Sc,Zr)$ precipitates. These primary $Al_3(Sc,Zr)$ particles were majorly located in the equiaxed grain zones and tended to be distributed within the grains. For the rapid cooling rate of LPBF, the primary $Al_3(Sc,Zr)$ precipitates concentrated at the boundaries of melt pool or remelt zones, promoting the fine equiaxed grain formation. Additionally, the rapid solidification rates produced a non-equilibrium solidification and supersaturated matrix. From the EDS results, the α(Al) matrix contained about 3.95 wt.% of Mg and 1.70 wt.% of Mn.

The SAED in Fig. 11 further identifies that above secondary phase Sc and Zr enriched particles demonstrated a cubic ordered $L1_2$ structure. The SAED pattern was carried out along $[110]_{Al}$, revealing the (100) type superlattice reflection which could be ascribed to $Al_3(Sc,Zr)$ phase. Thus, primary $L1_2$-$Al_3(Sc,Zr)$ phase could be confirmed, as presented in Fig. 11(b). Moreover, a high lattice coherent interface was also confirmed between $Al_3(Sc,Zr)$ phase and the neighboring α(Al) matrix. Generally, primary $Al_3(Sc,Zr)$ particles could be produced from the α(Al) matrix under equilibrium condition. Whereas, the precipitate behavior of $Al_3(Sc,Zr)$ in LPBF would rely on the non-equilibrium solidification and temperature of molten pool [12,15]. During LPBF, primary $Al_3(Sc,Zr)$ particles tend to be significantly suppressed due to the ultrafast solidification rate (10^6−10^7 K/s). However, the residual primary $Al_3(Sc,Zr)$ phase could form near the melt pool bottom, in which the temperature is lower than the liquid temperature [15], acting as seed crystals due to the low energy barrier and promoting the grain refinement. In contrast, within the molten pool center, in which the temperature is higher than that at the bottom, the $Al_3(Sc,Zr)$ particles would be significantly suppressed owing to high temperature and the absence of residual $Al_3(Sc,Zr)$ substrate.

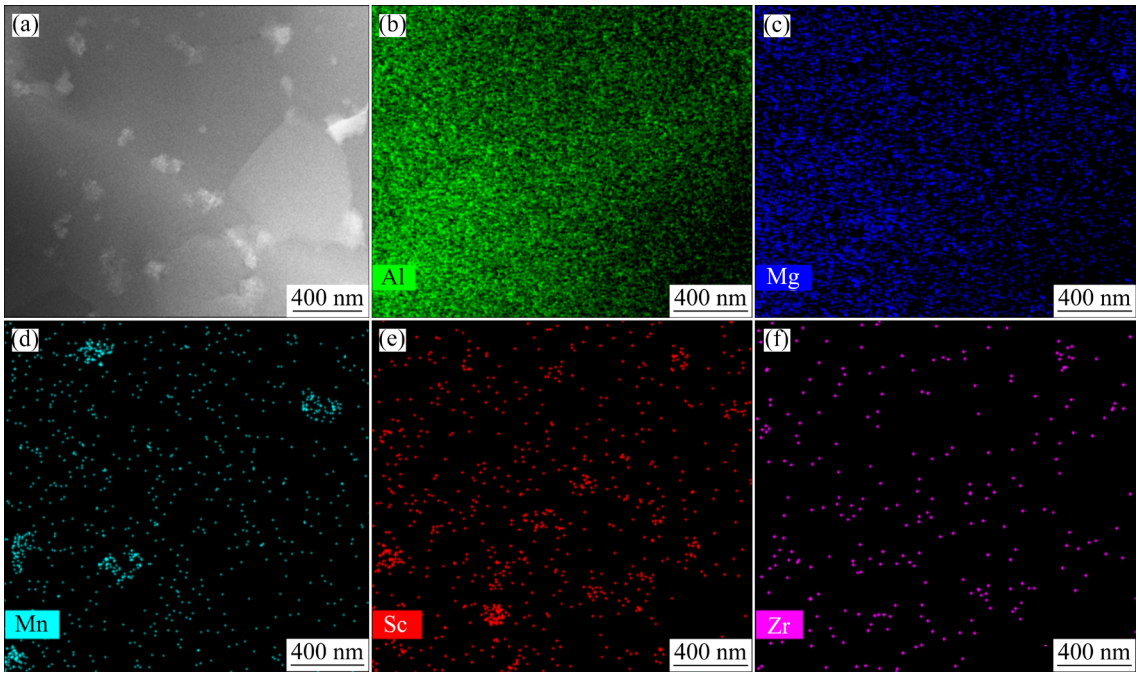

Fig. 10 (a) HAADF-STEM micrograph of sample fabricated at 1200 mm/s; (b−f) EDS mappings of Al, Mg, Mn, Sc and Zr, respectively

3.4 Mechanical performance in as-built condition

The engineering stress−strain curves of different specimens are plotted in Fig. 12(a) and the corresponding data are summarized in Table 3. As shown in Table 3, the yield strengths (YS) of the as-built specimens ranged from 327.8 to 357.5 MPa. The corresponding elongation to fracture was measured to be 24.79%, 24.05% and 22.60%, respectively. Therefore, the scanning speeds demonstrated a considerable effect on the tensile performance. Notably, all the tensile curves presented serrated flow, attributing to the Portevin–Le Chatelier (PLC) effect [29]. The PLC effect is ascribed to dynamic strain aging (DSA) interaction of Mg atoms and moving dislocations.

Additionally, it can also be observed that all specimens presented an obvious yield point with a subsequent yield plateau (Fig. 12(a)). This is different from traditional wrought Al alloys with nonlinear stress−strain curves [30]. The potential mechanism is the absence of moving dislocations in the fine grain zones, promoting the dynamic recovering through stimulating dislocations annihilating [31]. Table 3 also depicts the results of

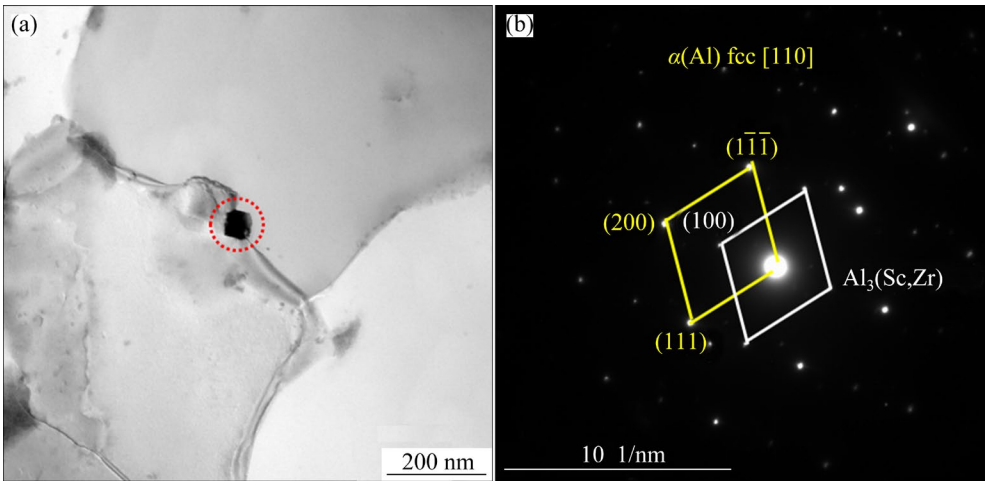

Fig. 11 (a) BF-TEM micrograph of fine grain zone: (b) Selected area electron diffraction (SAED) pattern of $L1_2$-$Al_3(Sc,Zr)$ precipitate

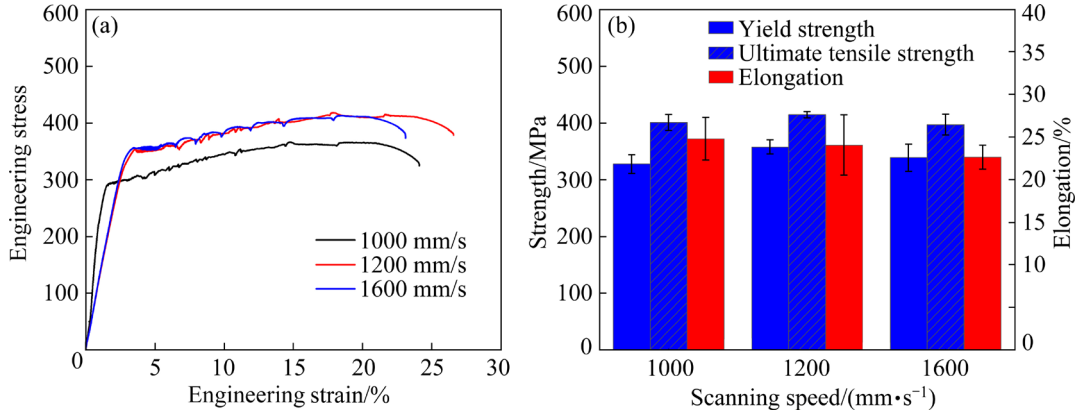

Fig. 12 Mechanical properties of samples fabricated at various scanning speeds: (a) Engineering stress−strain curves; (b) Tensile performance

Table 3 Mechanical performance of LPBF fabricated specimens at various scanning speeds

Scanning speed/ (mm·s^{-1})	Yield strength/ MPa	Ultimate tensile strength/ MPa	Elongation (El)/%	Microhardness (HV)
1000	327.8±16.5	400.6±13.6	24.79±2.52	106.7±3.0
1200	357.5±12.5	414.6±5.1	24.05±3.59	116.8±3.5
1600	338.9±23.7	396.8±18.6	22.60±1.42	116.7±3.2

microhardness at various scanning speeds. The most dense sample (v=1200 mm/s) demonstrated a microhardness value of $HV_{0.2}$ 117, which was larger than that of the other samples. Notably, the microhardness was dependent on the scanning speeds. The average microhardness value identified an obvious enhancement from $HV_{0.2}$ (106.7±3.0) to $HV_{0.2}$ (116.8±3.5) as the scanning speed increased from 1000 to 1200 mm/s. The increment of microhardness could be ascribed to Al_3(Sc,Zr) particle formation [26]. Meanwhile, the limited fluctuation of microhardness might be attributed to the pore defects. It was summarized that both tensile properties and microhardness were strongly based on the precipitate behavior, which was majorly controlled by the scanning speeds. The fracture morphologies of as-built samples are presented in Fig. 13, elucidating the plastic deformation behavior and fracture mechanism. Dimples were found in all specimens, showing a ductile rupture mode.

Furthermore, the fracture morphology images at low and high magnification were very similar. Numerous fine dimples could be found on the fracture surface, indicating excellent elongation to break. Notably, when the scanning rate increased to 1200 mm/s, the number of uniform and submicron dimples decreased while the proportion of smooth planes increased, indicating a reduction of elongation to break, which is consistent with the elongation data in Table 3. Moreover, some pores could be found on the fracture surface (Fig. 13(a)), which might come from enlarged pores formed by gas entrapped in the matrix or by small-sized invisible pores during deformation [32]. These pores could become the origin of cracks during tensile deformation and extend to the surrounding area, contributing to fracture. It is noteworthy that no visible pores were found on the fracture surface of sample manufactured at a scanning rate of 1200 mm/s. This further confirms that 1200 mm/s is the optimum scanning rate for fabricating high-density and high-performance samples in the current study.

3.5 Microstructure and mechanical performance evolution after heat treatment

Figure 14 depicts XRD patterns corresponding to the different specimens before and after heat treatment. It can be found that, within the resolution

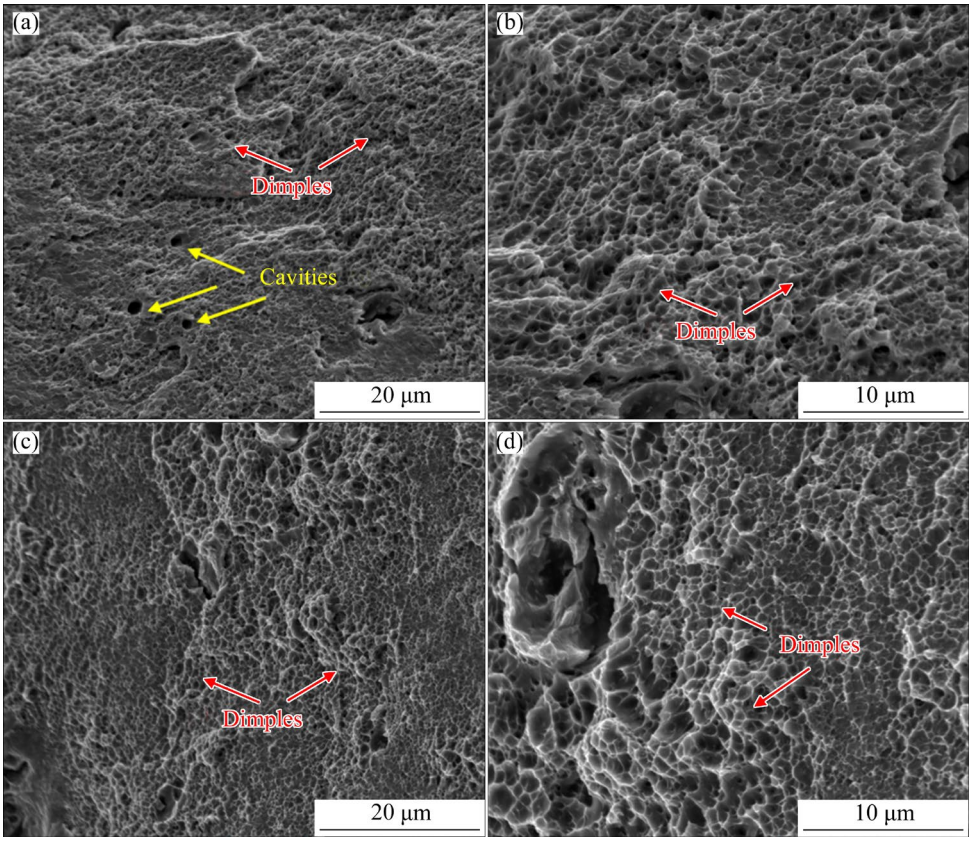

Fig. 13 Fracture characteristics at different scanning speeds: (a, b) 1000 mm/s; (c, d) 1200 mm/s

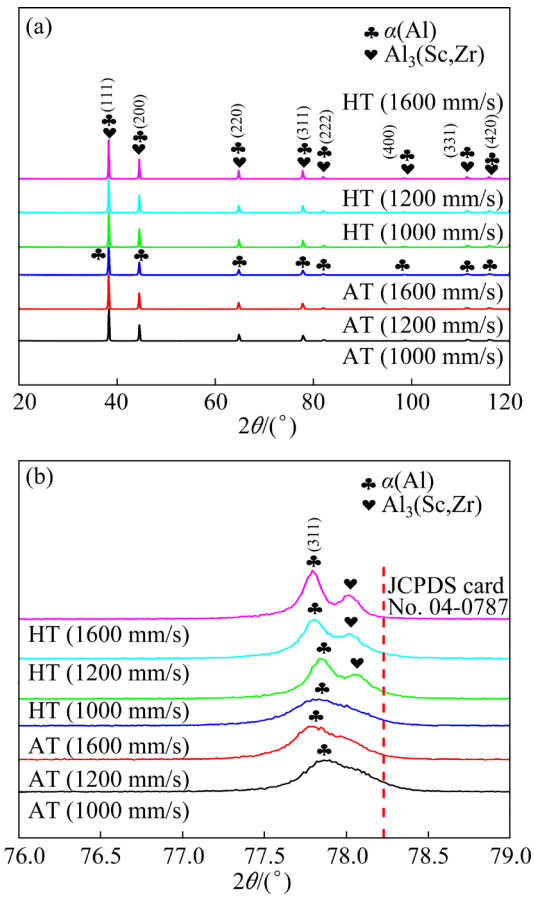

Fig. 14 XRD patterns of different samples (AT−As-built; HT−Heat-treated)

of XRD detection, the only detectable phase is α(Al) in as-built samples based on JCPDS Card No. 04-0787. Whereas, a small proportion of Al_3(Sc,Zr) phase could be recognized in heat-treated samples, as the diffraction peaks of Al_3(Sc,Zr) were observed. This indicated that the secondary Al_3(Sc,Zr) phase precipitated out during the heat treatment. Thus, the heat-treated sample majorly consisted of some α(Al) and Al_3(Sc,Zr) phases, which have also been identified in previous works [10].

Generally, the rapid cooling promoted non-equilibrium solidification and solubility of Sc and Zr, etc [33]. During the non-equilibrium solidification of LPBF, some primary Al_3(Sc,Zr) phases also formed. However, the content of these Al_3(Sc,Zr) phases in as-built specimens was limited owing to the rapid solidification rate (10^6 K/s), resulting in the invisible diffraction peaks attributed to Al_3(Sc,Zr) phase. In contrast, the solubility reduced accordingly during heat treatment, producing numerous secondary Al_3(Sc,Zr) particles while maintaining high coherency with the α(Al) matrix. The diffraction peaks of Al_3(Sc,Zr) in the heat-treated specimens could be detected due to the content increase of Al_3(Sc,Zr). Figure 14(b) further presents a magnified view of the (311) diffraction peak. From the magnified image, the (311) diffraction peak of heat-treated sample deflected to a lower angle compared with as-built sample. Due to the high solidification rate, large residual stresses were accumulated inside the part, which in turn contributed to the lattice distortion. As a result, the lattice distortion led to a shift of the diffraction peaks. However, the residual stresses were effectively released during heat treatment [34]. Thereby, the diffraction peak shifted to the left owing to the effective reduction of residual stress within heat-treated specimens.

The microstructural feature of heat-treated sample was further studied via high-magnification TEM (Fig. 15). Figures 15(a−c) present dark-field micrographs of fine and columnar grain zones. The heat-treated specimen was characterized by many secondary phase particles and high-density dislocations that were similar with the as-built specimen. After heat treatment, numerous nano-particles with mean size of (3.55±1.12) nm were formed from the supersaturated α(Al) matrix. The phase structure identification of these nanoparticles was further carried out by SAED analysis and the result is depicted in Fig. 15(d). The SAED pattern was recorded along $[001]_{Al}$ and the superlattice spots could be ascribed to fcc structure of Al_3(Sc,Zr). It was further confirmed that the Al_3(Sc,Zr) phase showed a high coherency with the α(Al) matrix. Generally, Sc and Zr were trapped in the supersaturated matrix of as-built samples attributing to a non-equilibrium solidification process. Because of the limited solubility, Sc and Zr solutes would precipitate out from the supersaturated matrix during heat treatment, producing Al_3(Sc,Zr) phase and promoting precipitation strengthening. This is also in line with the above XRD results, demonstrating the formation of secondary Al_3(Sc,Zr) phase within heat-treated specimens.

Figure 16 plots the tensile engineering stress−strain curves of samples before and after heat treatment and the tensile data are presented in Table 4. Obviously, the tensile performance of as-built samples could be further enhanced by post

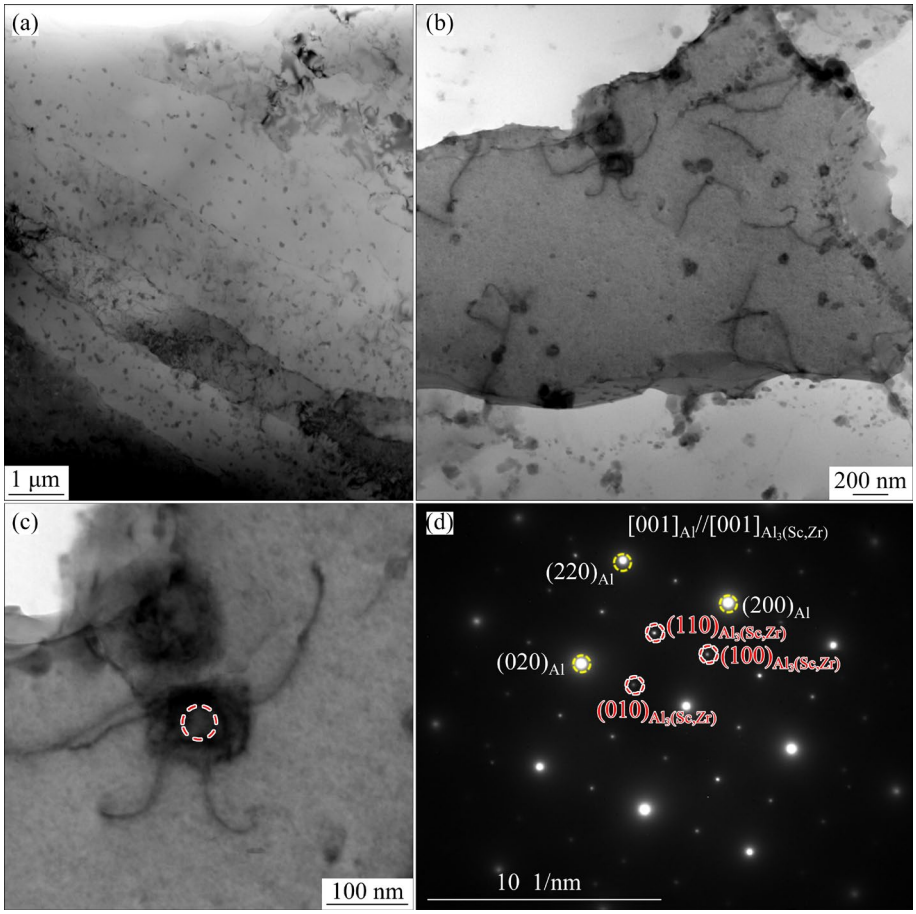

Fig. 15 (a) HAADF-STEM micrographs of heat-treated sample fabricated at 1200 mm/s; (b, c) HAADF-STEM micrograph at high magnification; (d) SAED pattern demonstrating high coherency between $Al_3(Sc,Zr)$ phase and α(Al) matrix

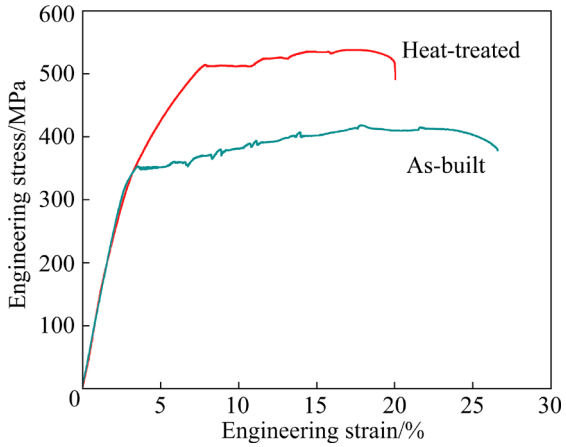

Fig. 16 Tensile engineering stress−strain curves of as-built and heat-treated samples fabricated at 1200 mm/s

heat treatment. Notably, the room temperature yield strength (YS) raised from (357.5±12.5) to (513.1±1.3) MPa, and ultimate tensile strength (UTS) from (414.6±5.1) to (539.2±1.5) MPa after heat treatment. Meanwhile, the elongation to break (El) reached (21.27±1.23)% even after heat

Table 4 Mechanical performance of samples under various conditions

Condition	Hardness ($HV_{0.2}$)	YS/MPa	UTS/MPa	El/%
As-built	116.8±3.5	357.5±12.5	414.6±5.1	24.05±3.59
Heat-treated	152.0±2.6	513.1±1.3	539.2±1.5	21.27±1.23

treatment, indicating its potential to process high-performance Al−Mg−Sc−Zr parts. The present Al−Mg−Sc−Zr alloy demonstrates outstanding strength and sound ductility that is much better than Sc-free Addalloy (Al−Mg−Zr, UTS=(382±5) MPa) [24]. Furthermore, its tensile performance is equal to commercialized high-strength 2××× and 7××× series Al alloys processed by traditional wrought techniques (UTS=(393−538) MPa) [30,35]. In addition, the work hardening ability of Al−Mg−Sc−Zr alloy was moderate and the PLC effect of heat-treated sample was less significant, as presented in Fig. 16. The reason could be the

depletion of solute and the formation of secondary phase particles during heat treatment.

The significant mechanical performance enhancement of heat-treated samples could be ascribed to the following mechanisms. The first is the high printability and the elimination of hot crackings. Generally, the hot crackings were considered to be the most serious threat to the LPBF fabricated parts. They could rapidly propagate and thus lead to sudden and premature break under tensile loading. The production of a refined heterogeneous microstructure also resulted in the strength improvement owing to grain boundary strengthening. Additionally, the extent of solid solubility in rapid solidification of LPBF led to strength enhancement, while the precipitation strengthening would be attributed to either dislocation shear of fine precipitates or dislocation bypassing via larger precipitates.

4 Discussion

4.1 Thermal behavior at different scanning speeds

As revealed by ZHANG et al [18], the densification and microstructure features of LPBF manufactured samples primarily relied on the thermal behavior and temperature gradients within the melt pool. And the mechanical performance was further determined by the microstructure features. Based on their finite element results, the size and temperature in the melt pool changed with various scanning speeds. As a result, the highest temperature and lifetime of molten pool both decreased with the increment of scanning speed. Meanwhile, the depth of molten pool was significantly decreased. Therefore, the temperature, lifetime and depth of melt pool are all decreased with the increment of scanning speed. Notably, the solidification microstructure of Al−Mg−Sc−Zr alloy (grain morphologies and precipitation behavior) is governed by following factors: (1) thermal gradient (G) direction and magnitude, and (2) the solidification rate (R). G can be calculated as [36]

$$G=\left|\frac{\partial T}{\partial x}\boldsymbol{i}+\frac{\partial T}{\partial y}\boldsymbol{j}+\frac{\partial T}{\partial z}\boldsymbol{k}\right| \tag{2}$$

where T represents temperature; $\boldsymbol{i}$, $\boldsymbol{j}$ and $\boldsymbol{k}$ are the unit vectors at three directions, respectively.

R is correlated with scanning speed (V) [37]:

$$R=|V|\cos\theta' \tag{3}$$

where θ' represents the angle of heat flow and laser scanning direction. The G reached a maximum value at the bottom of molten pool and reduced rapidly with the continuity of solidification. However, the R demonstrated the opposite tendency, the value was 0 at the bottom of molten pool and increased rapidly as the solidification continued. This difference in thermal behavior at various scanning speeds played a significant role in the microstructure formation.

4.2 Bimodal grain microstructure formation

Generally, equiaxed grains microstructure can decrease the strain concentration, providing a strategy to significantly enhance the strain accommodation ability during deforming [38]. The classical theory of solidification identifies that the production of equiaxial grain is stimulated by low thermal gradients (G) and high growing rates (R), which is a small G/R value [39]. Whereas, the level of G is usually too large to satisfy the critical situation of equiaxial grain formation during solidification of LPBF. This in turn contributes to large G/R values and thereby promotes epitaxial growth of columnar grains, as presented in Fig. 9(a). Notably, a high density of nucleation sites within melt pool was not considered in the above analysis. According to the theory of columnar-to-equiaxed transition (CET) [40], if molten pools contained sufficient nucleation sites, heterogeneous nucleation ahead of solid/liquid interfaces could be stimulated, expressed as follows:

$$\frac{G^{n'}}{V}=a'\left\{\sqrt[3]{\frac{-4\pi N_0}{3\ln[1-\phi]}}\cdot\frac{1}{n'+1}\right\}^{n'} \tag{4}$$

where a' and n' represent constants; N_0 and ϕ are nucleation particle density and equiaxed grain volume fraction, respectively. Generally, the precipitate behavior of $Al_3(Sc,Zr)$ was dependent on scanning speed. The solidification rates and precipitation behavior might be various under different scanning speeds. During the solidification of current Al−Mg−Sc−Zr alloy, the large amount of primary $Al_3(Sc,Zr)$ phase demonstrates a small lattice mismatch with α(Al), providing low energy-barrier nucleating sites ahead of solidification interfaces and promoting the equiaxed grains formation [35]. Thus, when more nucleation agents were introduced to the molten pool, the value of N_0 rose and adequate nucleation sites

promoted the CET, contributing to equiaxed grains structure formation, as presented in Fig. 9(a), despite large G/R ratio.

Actually, precipitation behavior of primary $Al_3(Sc,Zr)$ phase relies on the temperature [39]. As revealed by the numerical simulation results of SPIERINGS et al [41], the temperature at molten pool center regions can surpass 1500 °C during melting process, contributing to the full dissolution of $Al_3(Sc,Zr)$ particles. Based on the equilibrium phase diagram, the primary $Al_3(Sc,Zr)$ particles in molten pool center areas will be suppressed during subsequent solidification because of the high solidification rate [12], leading to epitaxial growing of columnar grains. Meanwhile, equiaxed grains can form near molten pool boundaries in which the temperature is lower than that in molten pool center and $Al_3(Sc,Zr)$ particles can survive as heterogeneous nucleation sites. Therefore, the intrinsic features of LPBF commonly contribute to a bimodal grain microstructure. Notably, the influence of other secondary phases on columnar-to-equiaxed transition can be neglected owing to greater lattice mismatch compared with $Al_3(Sc,Zr)$ phase.

4.3 Strengthening and toughing mechanism

As grain boundary strengthening potential is limited, the further strength increment of heat-treated samples should be attributed to the precipitate strengthening of secondary $Al_3(Sc,Zr)$ particles. Firstly, the number density of secondary $Al_3(Sc,Zr)$ particles would be dependent on the heat treatment because the rapid solidification could only effectively suppress primary $Al_3(Sc,Zr)$ phase during LPBF process. Additionally, due to the depletion of Sc and Zr near the melt pool bottom, remelting would reduce secondary $Al_3(Sc,Zr)$ phase during the building of adjacent scanning track and deposition layer [42]. Thereby, secondary $Al_3(Sc,Zr)$ phase might mainly come from the heat treatment process. Secondly, the supersaturated matrix would undergo a repetitive thermal cycle in building process, promoting the formation of limited secondary $Al_3(Sc,Zr)$ phase. This is also identified by the TEM result as presented in Fig. 11(a). Limited pea-like secondary $Al_3(Sc,Zr)$ nano-particles can be found. A similar result was also revealed at low scanning speed [43]. As demonstrated by WANG et al [44], secondary Al_3Sc and Al_3Zr precipitates in Al−5Mg−2Li−0.2Sc−0.2Zr (wt.%) alloy started to precipitate during the isochronal aging at 250 and 450 °C, respectively. Generally, the precipitation strengthening mainly relies on the square root of particle number. Owing to the high number of secondary $Al_3(Sc,Zr)$ phase formation during heat treatment, the precipitation strengthening of heat-treated samples is expected to be improved.

Moreover, the most primary $Al_3(Sc,Zr)$ phase was effectively suppressed owing to the rapid solidification of LPBF technique [12,15,43], and only a small amount of residual $Al_3(Sc,Zr)$ phase could be produced near molten pool boundary zones with the lower temperature than the liquid temperature (Fig. 8(d)). This can effectively inhibit the microvoids formation due to the stress concentration from secondary phase and matrix, benefiting for absorbing more energies during cracking initiation and propagation. Furthermore, it is worth noting that strain accommodation ability between equiaxed grain and columnar grain is excellent [45]. Thereby, the strain gradients could produce a beneficial hardening effect, improving strain hardening ability and inducing more energy absorption during deformation. Additionally, the excellent strain hardening ability of columnar grains can also significantly prevent the further propagation of microvoids and bear more plastic deformation.

5 Conclusions

(1) The densification behavior of Al−Mg−Sc−Zr samples was dependent on laser power, scanning speed and resultant energy densities. The highly dense and crack-free parts could be processed in a wide printing window, identifying excellent printability of Al−Mg−Sc−Zr alloy.

(2) The XRD diffraction peaks of as-built samples demonstrated an obvious (200) texture in comparison with (111) texture within raw powders, identifying a marked texture transformation. Furthermore, a prominent shift of diffraction peak to a lower angle and an increase of lattice plane distance were observed in as-built samples. And the Mg volatilization in as-built samples contributed to the decrease of lattice plane distance compared with raw powders.

(3) LPBF process provided a promising

technique for obtaining fine grain microstructure owing to heterogeneous nucleation of $Al_3(Sc,Zr)$ precipitates, which can effectively prevented the cracking initiation and propagation. The precipitate behavior of $Al_3(Sc,Zr)$ particles was dependent on the scanning speed.

(4) The effects of scanning speed on tensile performance were distinct. The ultimate tensile strength of Al−Mg−Sc−Zr alloy ranged from 396.8 to 414.6 MPa before heat treatment. After post heat treatment, the YS increased to (513.1±1.3) MPa, while the UTS increased from (414.6±5.1) to (539.2±1.5) MPa. The significant improvement in YS and UTS of heat-treated samples could be majorly ascribed to the formation of the secondary $Al_3(Sc,Zr)$ nanoparticles.

CRediT authorship contribution statement

Xiang LI: Conceptualization, Methodology, Formal analysis, Investigation, Data curation, Writing − Original draft; **Zheng-jiang GAO**: Formal analysis, Writing – Review & editing; **Yun-zhong LIU**: Resources, Writing − Review & editing, Supervision.

Declaration of competing interest

The authors declare that they have no known competing financial interests or personal relationships that could have appeared to influence the work reported in this paper.

Acknowledgments

The authors would like to thank the support of the Research and Development Program in Key Areas of Guangdong Province, China (No. 2019B090907001), the Science and Technology Program of Guangdong Province, China (No. 2014B010129002), and the National Key R&D Program of China (No. 2017YFB0305800).

References

[1] TAN Chao-lin, ZOU Ji, WANG Di, MA Wen-you, ZHOU Ke-song. Duplex strengthening via SiC addition and in-situ precipitation in additively manufactured composite materials [J]. Composites, Part B, 2022, 236: 109820.

[2] LI Rui-di, WANG Min-bo, LI Zhi-ming, CAO Peng, YUAN Tie-chui, ZHU Hong-bin. Developing a high-strength Al−Mg−Si−Sc−Zr alloy for selective laser melting: Crack-inhibiting and multiple strengthening mechanisms [J]. Acta Materialia, 2020, 193: 83−98.

[3] GRIFFITHS S, CROTEAU J R, ROSSELL M D, ERNI R, DE L A, VO N Q, DUNAND D C, LEINENBACH C. Coarsening- and creep resistance of precipitation-strengthened Al−Mg−Zr alloys processed by selective laser melting [J]. Acta Materialia, 2020, 188: 192−202.

[4] WANG Zi-hong, LIN Xin, WANG Jing-feng, KANG Nan, HU Yun-long, WANG Dan-qian, LI Hong-yun, HUANG Wei-dong, PAN Fu-shen. Remarkable strength−impact toughness conflict in high-strength Al−Mg−Sc−Zr alloy fabricated via laser powder bed fusion additive manufacturing [J]. Additive Manufacturing, 2022, 59: 103093.

[5] JIA Qing-bo, ROMETSCH P, KÜRNSTEINER P, CHAO Qi, HUANG Ai-jun, WEYLAND M, BOURGEOIS L, WU Xin-hua. Selective laser melting of a high strength Al−Mn−Sc alloy: Alloy design and strengthening mechanisms [J]. Acta Materialia, 2019, 171: 108−118.

[6] TAN Qi-yang, ZHANG Jing-qi, SUN Qiang, FAN Zhi-qi, LI Gan, YIN Yu, LIU Yin-gang, ZHANG Ming-xing. Inoculation treatment of an additively manufactured 2024 aluminium alloy with titanium nanoparticles [J]. Acta Materialia, 2020, 196: 1−16.

[7] TAN Qi-yang, LIU Yin-gang, FAN Zhi-qi, ZHANG Jing-qi, YIN Yu, ZHANG Ming-xing. Effect of processing parameters on the densification of an additively manufactured 2024 Al alloy [J]. Journal of Materials Science & Technology, 2020, 58: 34−45.

[8] QI Yang, ZHANG Hu, NIE Xiao-jia, HU Zhi-heng, ZHU Hai-hong, ZENG Xiao-yan. A high strength Al−Li alloy produced by laser powder bed fusion: Densification, microstructure, and mechanical properties [J]. Additive Manufacturing, 2020, 35: 101346.

[9] BAHL S, SISCO K, YANG Ying, THESKA F, PRIMIG S, ALLARD L F, MICHI R A, FANCHER C, STUMP B, DEHOFF R, SHYAM A, PLOTKOWSKI A. Al−Cu−Ce(−Zr) alloys with an exceptional combination of additive processability and mechanical properties [J]. Additive Manufacturing, 2021, 48: 102404.

[10] ZHANG Han, GU Dong-dong, DAI Dong-hua, MA Cheng-long, LI Yu-xin, CAO Meng-zhen, LI Shu-hui. Influence of heat treatment on corrosion behavior of rare earth element Sc modified Al−Mg alloy processed by selective laser melting [J]. Applied Surface Science, 2020, 509: 145330.

[11] WANG Zi-hong, LIN Xin, KANG Nan, CHEN Jing, TAN Hua, FENG Zhe, QIN Ze-hao, YANG Hai-ou, HUANG Wei-dong. Laser powder bed fusion of high-strength Sc/Zr-modified Al−Mg alloy: Phase selection, microstructural/mechanical heterogeneity, and tensile deformation behavior [J]. Journal of Materials Science & Technology, 2021, 95: 40−56.

[12] WANG Zi-hong, LIN Xin, KANG Nan, HU Yun-long, CHEN Jing, HUANG Wei-dong. Strength-ductility synergy of selective laser melted Al−Mg−Sc−Zr alloy with a heterogeneous grain structure [J]. Additive Manufacturing, 2020, 34: 101260.

[13] FANG Hong-jie, LIU Hui, YAN Yang, LUO Xier, XU Xiang-chun, CHU Xin, LU Yu-jiao, YU Kun, WANG Dian-gang. Evolution of texture, microstructure, tensile strength and corrosion properties of annealed Al−Mg−Sc−Zr alloys [J]. Materials Science and Engineering A, 2021, 804:

140682.

[14] SHI Yun-jia, YANG Kun, KAIRY S K, PALM F, WU Xin-hua, ROMETSCH P A. Effect of platform temperature on the porosity, microstructure and mechanical properties of an Al−Mg−Sc−Zr alloy fabricated by selective laser melting [J]. Materials Science and Engineering A, 2018, 732: 41−52.

[15] SPIERINGS A B, DAWSON K, HEELING T, UGGOWITZER P J, SCHÄUBLIN R, PALM F, WEGENER K. Microstructural features of Sc- and Zr-modified Al−Mg alloys processed by selective laser melting [J]. Materials & Design, 2017, 115: 52−63.

[16] SCHMIDTKE K, PALM F, HAWKINS A, EMMELMANN C. Process and mechanical properties: Applicability of a scandium modified Al-alloy for laser additive manufacturing [J]. Physics Procedia, 2011, 12: 369−374.

[17] SPIERINGS A B, DAWSON K, KERN K, PALM F, WEGENER K. SLM-processed Sc- and Zr-modified Al−Mg alloy: Mechanical properties and microstructural effects of heat treatment [J]. Materials Science and Engineering A, 2017, 701: 264−273.

[18] ZHANG Han, DAI Dong-hua, YUAN Lu-hao, LIU He, GU Dong-dong. Temperature gradient induced tough-brittle transition behavior of a high-strength Al−4.2Mg−0.4Sc−0.2Zr alloy fabricated by laser powder bed fusion additive manufacturing [J]. Additive Manufacturing, 2023, 73: 103655.

[19] ZHOU Le, HYER H, CHANG Jin-fa, MEHTA A, HUYNH T, YANG Yang, SOHN Y. Microstructure, mechanical performance, and corrosion behavior of additively manufactured aluminum alloy 5083 with 0.7 and 1.0 wt.% Zr addition [J]. Materials Science and Engineering A, 2021, 823: 141679.

[20] GU Dong-dong, HAGEDORN Y C, MEINERS W, MENG Guang-bin, BATISTA R J S, WISSENBACH K, POPRAWE R. Densification behavior, microstructure evolution, and wear performance of selective laser melting processed commercially pure titanium [J]. Acta Materialia, 2012, 60(9): 3849−3860.

[21] GU Dong-dong, RAO Xiang-wei, DAI Dong-hua, MA Cheng-long, XI Li-xia, LIN Kai-jie. Laser additive manufacturing of carbon nanotubes (CNTs) reinforced aluminum matrix nanocomposites: Processing optimization, microstructure evolution and mechanical properties [J]. Additive Manufacturing, 2019, 29: 100801.

[22] WEINGARTEN C, BUCHBINDER D, PIRCH N, MEINERS W, WISSENBACH K, POPRAWE R. Formation and reduction of hydrogen porosity during selective laser melting of AlSi10Mg [J]. Journal of Materials Processing Technology, 2015, 221: 112−120.

[23] ABOULKHAIR N T, EVERITT N M, ASHCROFT I, TUCK C. Reducing porosity in AlSi10Mg parts processed by selective laser melting [J]. Additive Manufacturing, 2014, 1: 77−86.

[24] CROTEAU J R, GRIFFITHS S, ROSSELL M D, LEINENBACH C, KENEL C, JANSEN V, SEIDMAN D N, DUNAND D C, VO N Q. Microstructure and mechanical properties of Al−Mg−Zr alloys processed by selective laser melting [J]. Acta Materialia, 2018, 153: 35−44.

[25] THIJS L, MONTERO S M L, WAUTHLE R, XIE Qing-ge, KRUTH J P, VAN H J. Strong morphological and crystallographic texture and resulting yield strength anisotropy in selective laser melted tantalum [J]. Acta Materialia, 2013, 61: 4657−4668.

[26] ZHANG Han, GU Dong-dong, YANG Jian-kai, DAI Dong-hua, ZHAO Tong, HONG Chen, GASSER A, POPRAWE R. Selective laser melting of rare earth element Sc modified aluminum alloy: Thermodynamics of precipitation behavior and its influence on mechanical properties [J]. Additive Manufacturing, 2018, 23: 1−12.

[27] LI Rui-di, WANG Min-bo, YUAN Tie-chui, SONG Bo, CHEN Chao, ZHOU Ke-chao, CAO Peng. Selective laser melting of a novel Sc and Zr modified Al−6.2Mg alloy: Processing, microstructure, and properties [J]. Powder Technology, 2017, 319: 117−128.

[28] ZHANG Han, GU Dong-dong, DAI Dong-hua, MA Cheng-long, LI Yu-xin, PENG Ruo-lin, LI Shu-hui, LIU Gang, YANG Bi-qi. Influence of scanning strategy and parameter on microstructural feature, residual stress and performance of Sc and Zr modified Al−Mg alloy produced by selective laser melting [J]. Materials Science and Engineering A, 2020, 788: 139593.

[29] WANG Zi-hong, LIN Xin, KANG Nan, CHEN Jing, TANG Yao, TAN Hua, YU Xiao-bin, YANG Hai-ou, HUANG Wei-dong. Directed energy deposition additive manufacturing of a Sc/Zr-modified Al−Mg alloy: Effect of thermal history on microstructural evolution and mechanical properties [J]. Materials Science and Engineering A, 2021, 802: 140606.

[30] WANG Yan-fang, LIN Xin, KANG Nan, WANG Zi-hong, LIU Yu-xi, HUANG Wei-dong. Influence of post-heat treatment on the microstructure and mechanical properties of Al−Cu−Mg−Zr alloy manufactured by selective laser melting [J]. Journal of Materials Science & Technology, 2022, 111: 35−48.

[31] JIA Qin-gbo, ZHANG Fan, ROMETSCH P, LI Jing-wei, MATA J, WEYLAND M, BOURGEOIS L, SUI Man-ling, WU Xin-hua. Precipitation kinetics, microstructure evolution and mechanical behavior of a developed Al−Mn−Sc alloy fabricated by selective laser melting [J]. Acta Materialia, 2020, 193: 239−251.

[32] GAO C, WU W, SHI J, XIAO Z, AKBARZADEH A H. Simultaneous enhancement of strength, ductility, and hardness of TiN/AlSi10Mg nanocomposites via selective laser melting [J]. Additive Manufacturing, 2020, 34: 101378.

[33] BI Jiang, LEI Zheng-long, CHEN Yan-bin, CHEN Xi, TIAN Ze, LU Nan-nan, QIN Xi-kun, LIANG Jing-wei. Microstructure, tensile properties and thermal stability of AlMgSiScZr alloy printed by laser powder bed fusion [J]. Journal of Materials Science & Technology, 2021, 69: 200−211.

[34] DENG Qing-chen, WU Yu-juan, WU Qian-ye, XUE Yan-ting, ZHANG Yu, PENG Li-ming, DING Wen-jiang. Microstructure evolution and mechanical properties of a high-strength Mg−10Gd−3Y−1Zn−0.4Zr alloy fabricated by laser powder bed fusion [J]. Additive Manufacturing, 2022, 49: 102517.

[35] MARTIN J H, YAHATA B D, HUNDLEY J M, MAYER J A, SCHAEDLER T A, POLLOCK T M. 3D printing of

high-strength aluminium alloys [J]. Nature, 2017, 549(7672): 365−369.

[36] WEI H L, MAZUMDER J, DEBROY T D. Evolution of solidification texture during additive manufacturing [J]. Science Report, 2015, 5: 16446.

[37] GONG Hai-jun, RAFI K, GU Heng-feng, STARR T, STUCKER B. Analysis of defect generation in Ti−6Al−4V parts made using powder bed fusion additive manufacturing processes [J]. Additive Manufacturing, 2014, 1: 87−98.

[38] XIAO Xiao, GUO You-jie, ZHANG Rui-feng, BAYOUMY Dina, SHEN Hao-peng, LI Jin-feng, GAN Ke-fu, ZHANG Kai, ZHU Yu-man, HUANG Ai-jun. Achieving uniform plasticity in a high strength Al−Mn−Sc based alloy through laser-directed energy deposition [J]. Additive Manufacturing, 2022, 60: 103273.

[39] YANG K V, SHI Yun-jia, PALM F, WU Xin-hua, ROMETSCH P. Columnar to equiaxed transition in Al−Mg(−Sc)−Zr alloys produced by selective laser melting [J]. Scripta Materialia, 2018, 145: 113−117.

[40] WANG Zhi-chao, WANG Xin-tian, CHEN Xu, QIU Chun-lei. Complete columnar-to-equiaxed transition and significant grain refinement in an aluminium alloy by adding Nb particles through laser powder bed fusion [J]. Additive Manufacturing, 2022, 51: 102615.

[41] SPIERINGS A B, DAWSON K, DUMITRASCHKEWITZ P, POGATSCHER S, WEGENER K. Microstructure characterization of SLM-processed Al−Mg−Sc−Zr alloy in the heat treated and HIPed condition [J]. Additive Manufacturing, 2018, 20: 173−181.

[42] WANG Zi-hong, LIN Xin, TANG Yao, KANG Nan, GAO Xue-hao, SHI Shuo-qing, HUANG Wei-dong. Laser-based directed energy deposition of novel Sc/Zr-modified Al−Mg alloys: Columnar-to-equiaxed transition and aging hardening behavior [J]. Journal of Materials Science & Technology, 2021, 69: 168−179.

[43] SPIERINGS A B, DAWSON K, UGGOWITZER P J, WEGENER K. Influence of SLM scan-speed on microstructure, precipitation of Al3Sc particles and mechanical properties in Sc- and Zr-modified Al−Mg alloys [J]. Materials & Design, 2018, 140: 134−143.

[44] WANG Yang, ZHANG Zhen, WU Rui-zhi, SUN Jian-feng, JIAO Yun-lei, HOU Le-gan, ZHANG Jing-huai, LI Xin-lin, ZHANG Mi-lin. Ambient-temperature mechanical properties of isochronally aged 1420-Sc−Zr aluminum alloy [J]. Materials Science and Engineering A, 2019, 745: 411−419.

[45] MA Evan, ZHU Ting. Towards strength–ductility synergy through the design of heterogeneous nanostructures in metals [J]. Materials Today, 2017, 20(6): 323−331.

激光粉末床熔融 Al−Mg−Sc−Zr 合金的显微组织和力学性能演变

李 响[1,2]，高正江[3]，刘允中[1,2]

1. 华南理工大学 广东省金属新材料制备与成形重点实验室，广州 510640；
2. 华南理工大学 国家金属材料近净成形工程技术研究中心，广州 510640；
3. 北京工业大学 新型功能材料教育部重点实验室，北京 100124

摘 要：采用激光粉末床熔融(LPBF)增材制造工艺制备 Al−Mg−Sc−Zr 合金，系统研究成形试样的致密化特征、物相组成、析出相演变和力学性能。此外，通过 X 射线衍射(XRD)和透射电子显微镜(TEM)分析热处理后的物相组成和析出相的演变。结果表明，当激光扫描速率由 1600 mm/s 降至 1000 mm/s，试样的极限拉伸强度(UTS)在 396.8~414.6 MPa 之间。经进一步热处理，屈服强度(YS)增加，达到(513.1±1.3) MPa，而 UTS 则从(414.6±5.1) MPa 增加到(539.2±1.5) MPa。合金力学性能的明显改善归因于二次 $Al_3(Sc,Zr)$析出相的形成。

关键词：增材制造；激光粉末床熔融；Al−Mg−Sc−Zr；析出行为；显微组织；力学性能

(Edited by Bing YANG)